Numerical modeling of ice behavior under high velocity impacts

J. Pernas-Sánchez, D.A. Pedroche, D. Varas, J. López-Puente *, R. Zaera

Department of Continuum Mechanics and Structural Analysis, Universidad Carlos III de Madrid, Avda. de la Universidad 30, 28911 Leganés, Madrid, Spain

ABSTRACT

In this work a constitutive relation for ice at high strain rates and an algorithm for its numerical integra tion are developed. This model is based on the Drucker Prager plasticity criteria, which allows a different behavior in tension and in compression. In addition a failure criteria, based on pressure cut offs, is imple mented to describe the ice damage. In order to validate the constitutive model, numerical simulations were compared with experimental results, in which ice cylinders were impacted against a steel plate, allowing the measurement of the contact load. Three different numerical solvers are used in order to ana lyze its performance to appropriately modeling the ice behavior.

1. Introduction

Aircraft structures may be subjected to a variety of environmen tal impact hazards. Radome, radar antenna, landing lights, canopy, windshield, lateral section or intake of the engine nacelle, turbine blades, wing or tail empennage leading edges are eventually tar gets of high velocity impact loading during flight, takeoff, and landing. Today, the risk of structural and system failures, as well as of occupant injuries, is well recognized in aircraft design. There are a number of different causes for these shocks. Together with bird strikes, hailstones are the most critical because of their high probability of occurrence and their consequences. Also the ice re leased from the edge of a propeller blade may impact the nacelle of the twin engine or the fuselage. In the field of spacecraft, ice pre sents one of the more serious debris impact threats to the Space Shuttle orbiter thermal protection systems. Ice that forms on the fuel lines of the external tank, if dislodged during flight, can impact orbiter tiles or the reinforced carbon carbon wing leading edge (Fasanella et al., 2006). Therefore, these structures should show tolerance to damage caused by ice impact, and their design should consider ice impact as a potential threat. Consequently, the mechanical behavior of ice has to be characterized through experimental test, and numerical tools models suitable for the sim ulation of ice at high strain rates have to be developed. Ice, how ever, is not a structural material, and commercial codes does not have appropriate models for it.

The mechanical behavior of ice has been widely studied for arctic ship transportation, oil and gas facilities, and for cold ocean or glacier research. All these studies refer to *Ih* ice, the most common ice in

earth, occurring when liquid water is cooled below 0 °C at ambient pressure. It can also deposit from vapor with no intervening liquid phase, such as in the accretion of glaze or rime ice at the airfoil of air planes. *Ih* ice possesses the hexagonal crystal structure reflected in the shape of snow flakes. The other crystal forms of ice are thermo dynamically stable only at high pressures. Deformation of ice in the previous fields occurs at low strain rates (10^{-7} to 10^{-1} s^{-1}) thus creep and quasi static experimental test are performed to gain knowledge about its behavior (Cole, 1988; Haynes, 1978; Gold, 1988; Schulson, 1990, 2001; Petrovic, 2003). These tests shown a noticeable influ ence of the formation conditions of ice, leading to single crystal or polycrystal columnar or granular structures with different grain sizes, on the mechanical properties. The presence of inclusions or air bubbles, acting as stress concentrators, also influences the mechan ical properties. Therefore, some researchers resort to ice manufac turing companies to make provision of a *standard* material. Young's modulus has been reported to be in the range of 9.7 11.2 GPa and Poisson's ratio varies from 0.29 to 0.32. Tensile strength varies be tween 0.7 and 3.1 MPa and depends on the specimen volume, follow ing a Weibull statistical distribution. Compressive strength ranges between 5 and 25 MPa. Some properties (such as compressive strength) are strongly modified by temperature as well, so experi mental results are commonly provided for a given set of pre defined temperatures (10, 20, 30, 40 °C). Ice shows brittle behavior in tension due to crack nucleation and cleavage. Like other brittle materials, confinement and pressure increases ductility and strength, the mechanism usually hypothesized being intergranular friction. However, a change to brittle compressive failure appears at strain rates higher than 10^{-2} s^{-1}.

Less attention has been paid to the study of ice at high strain rates. There are however some articles relating microstructure, temperature and strain rate with its response under compressive

* Corresponding author.
  E-mail address: jlpuente@ing.uc3m.es (J. López-Puente).

1

loads. Different devices were used to study the behavior at high strain rates: high speed universal testing machine up to $50\,s^{-1}$ (Jones, 1997; Combescure et al., 2011), drop weight tower up to $300\,s^{-1}$ (Fasanella et al., 2006) and split Hopkinson pressure bar up to $2600\,s^{-1}$ (Dutta, 1993; Kim and Keune, 2007; Shazly et al., 2009). The results suggest that the response at high strain rates appears to be independent of microstructure. As in quasi static conditions, strength increases with temperature decrease. The peak strength of ice has a steady increase up to strain rates having $10^3\,s^{-1}$ order of magnitude, and the relation seems to be conveniently approximated by a power law. Some authors (Kim et al., 2003; Pereira et al., 2006) launched cylindrical or spherical ice projectiles at ballistic velocities onto a rigid target supported by a dynamic load cell to measure the contact force during an impact event. The corresponding results have been later used by the same or other authors to validate numerical models. Regarding tensile behavior, experimental results (Petrovic, 2003) show brittle failure and a negligible influence of strain rate in the strength of ice.

Literature describing constitutive equations for the simulation of ice impact is likewise scarce. The most simple ones (Kim and Keune, 2000; Anghileri et al., 2005) used standard models available in commercial codes to describe the mechanical behavior of ice, J2 elastoplastic model with plastic strain failure and pressure failure; after failure the material behaves like a fluid carrying only hydro static pressures. Other authors (Park and Kim, 2010) used a J2 elastoplastic model with a tensile failure criterion, which assumes that failure occurs when the pressure becomes more tensile than the user specified hydrostatic cutoff stress; the deviatoric stress of the failed material is set to zero and stress remains at the cutoff pressure. The first constitutive equation specifically developed for ice deforming at high strain rates was that of Carney et al. (2006), who proposed a logarithmic strain rate sensitivity and pressure dependent strength. The model also considers different failure modes: critical value of the plastic strain, pressure cut off in compression and pressure cut off in tension. Combescure et al. (2011) used a constitutive equation based on the damage model of Mazars and modified it to allow degradation for compressive stress states and to include viscous effects. Well beyond the range of impact velocities distinctive of aircraft applications, Sherburn and Horstemeyer (2010) proposed and validated a constitutive model for the hypervelocity range based on the Bammann Chiesa Johnson rate and temperature dependent equation and on the Mie Gruniesen equation of state. In that work, ice is considered as a target instead of as projectile.

In this paper an original model to simulate the behavior of ice under impact conditions is described and validated. The model gathers the essential features of the mechanical behavior of ice at high strain rates, as deduced from the test performed by other authors, and presents the advantage that their parameters may be taken from the results of these experimental works. The model has been implemented in the commercial code LS DYNA (LSTC, 2010) and three different solvers (Lagrangian mesh, arbitrary Lagrangian Eulerian mesh and smoothed particles hydrodynamics) have been considered to reproduce the experimental data reported by Carney et al. (2006). Advantages and disadvantages of the three solvers have been evaluated. Additionally, once the material model was validated, the influence of the projectile slenderness in impact force has been studied, through a parametric study of projectile dimensions.

2. Ice numerical model description

In order to simulate the ice behavior under high strain rates, a constitutive equation based on the Drucker and Prager (1952) model has been proposed.

2.1. Material modeling

2.1.1. Hypoelastic approach

The motion of a deformable body can be described through the deformation gradient tensor $\mathbf{F}$. This tensor transforms an infinitesimal material vector $\mathbf{dX}$ into the corresponding spatial vector $\mathbf{dx}$, i.e.

$$\mathbf{dx} = \mathbf{F}\,\mathbf{dX} \tag{1}$$

To separate the recoverable and non recoverable contributions of the deformation gradient, the Kröner Lee multiplicative split of $\mathbf{F}$ is assumed (Kröner, 1959; Lee, 1969).

$$\mathbf{F} = \mathbf{F}^e \mathbf{F}^p \tag{2}$$

where $\mathbf{F}^e$ and $\mathbf{F}^p$ represent the reversible elastic deformation and inelastic deformation of the material, respectively. This decomposition implies the so called plastic intermediate configuration defined by $\mathbf{F}^{e\,-1}$, which is valid only locally. For impact applications, elastic strains (and rates) are commonly very small compared to unity or to plastic strains (and rates). With this restriction, we may arrive to the additive decomposition of the rate of deformation tensor in its corresponding elastic and plastic components, generally assumed for hypoelastic plastic materials (Nemat Nasser, 1982; Khan and Huang, 1995)

$$\mathbf{d} = \mathbf{d}^e + \mathbf{d}^p \tag{3}$$

2.1.2. Elastic behavior

Assuming the hypothesis of hypoelastic behavior, the elastic strain rate is provided by the following expression of Hooke's law

$$\boldsymbol{\sigma}^\nabla = \mathbf{C}:\mathbf{d}^e = \mathbf{C}:(\mathbf{d} - \mathbf{d}^p) \tag{4}$$

where $\boldsymbol{\sigma}^\nabla$ is an objective rate of the Cauchy stress tensor and $\mathbf{C}$ is the Hooke stress strain tensor defined by the elastic constants G and K.

2.1.3. Inelastic behavior

For the description of the inelastic behavior of ice, the model considers the experimental observations made by several authors (Schulson, 2001; Shazly et al., 2006, 2009), namely pressure dependence of strength, increase in compressive strength with strain rate, and residual strength after damage. Therefore, the model assumes a Drucker and Prager (1952) yield function to define the pressure dependence

$$f = \bar{\sigma} - (\sigma_{0y} + 3\alpha p) \tag{5}$$

where 3α is a parameter related to the internal friction angle of the material and σ_{0y} is the material cohesion (Fig. 1). $\bar{\sigma}$ is the equivalent stress defined as

$$\bar{\sigma} = \sqrt{\frac{3}{2}\mathbf{s}:\mathbf{s}} \tag{6}$$

$\mathbf{s}$ being the deviatoric stress tensor, and p the hydrostatic pressure defined as

$$p = \frac{\boldsymbol{\sigma}:\mathbf{1}}{3} \tag{7}$$

Both α and σ_{0y} parameters may be related with the uniaxial stress limits in compression σ_C and tension σ_T

$$\alpha = \frac{\sigma_C - \sigma_T}{\sigma_C + \sigma_T} \tag{8}$$

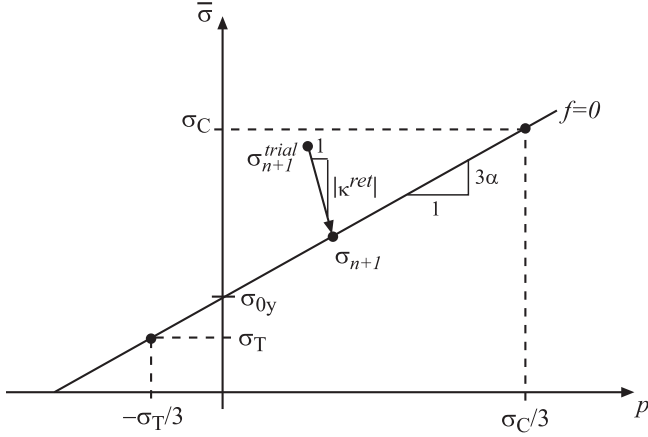$$\sigma_{0y} = \frac{2\sigma_C\sigma_T}{\sigma_C + \sigma_T} \tag{9}$$

Fig. 1. Yield locus in the $\{p, \bar{\sigma}\}$ space, and direction of stress return.

so that the Drucker–Prager yield surface is completely defined once σ_C and σ_T are known (Fig. 1). According to the experimental findings of several authors (Jones, 1982, 1997; Shazly et al., 2006; Kim and Keune, 2007), the compressive strength is dependent on strain rate; the same authors suggested that the viscous dependence is approximately linear in a log–log plot (see Fig. 2), so a power law with strain rate sensitivity m was proposed

$$\sigma_C\left(\dot{\bar{\varepsilon}}^p\right) = \sigma_{C0}\left(\frac{\dot{\bar{\varepsilon}}^p}{\dot{\varepsilon}_0}\right)^m \tag{10}$$

$\dot{\bar{\varepsilon}}^p$ being the equivalent plastic strain rate

$$\dot{\bar{\varepsilon}}^p = \sqrt{\frac{2}{3}\mathbf{d}^p : \mathbf{d}^p} \tag{11}$$

Regarding tensile behavior, as aforementioned, experimental results (Petrovic, 2003) show brittle failure and a negligible influence of strain rate in the strength of ice, so a constant value was chosen for σ_T.
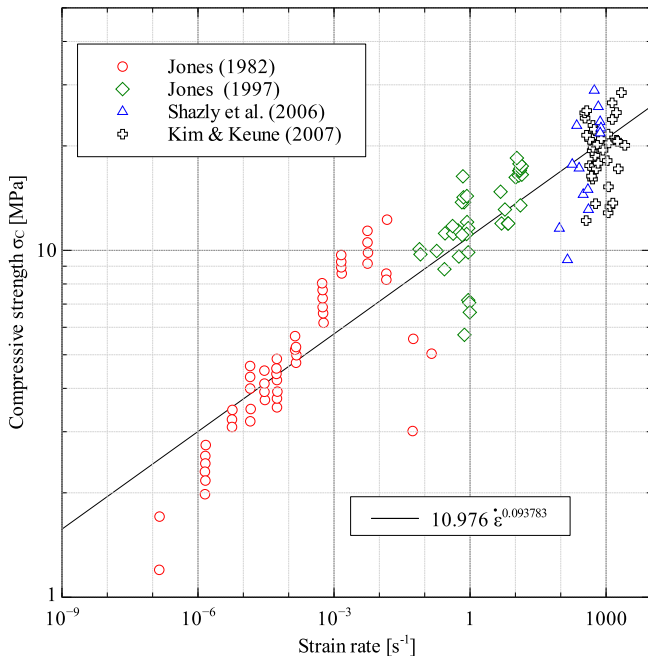

Fig. 2. Strain rate sensitivity of compressive strength of ice (Jones, 1982, 1997; Shazly et al., 2006; Kim and Keune, 2007).

To describe the inelastic flow, associative plasticity laws are often inappropriate since they overestimate the volumetric part of the plastic strain (Jirásek and Bažant, 2002). Therefore a non-associated plastic flow rule is chosen

$$\mathbf{d}^p = \dot{\lambda}\frac{\partial \Psi}{\partial \boldsymbol{\sigma}} = \dot{\lambda}\Psi_{\sigma} \tag{12}$$

where $\dot{\lambda}$ is the plastic multiplier, and the plastic potential Ψ is formally analogous to the yield function (Eq. (5)) but has a lower slope with the pressure α_Ψ

$$\Psi = \bar{\sigma} - (3\alpha_\Psi p + \Upsilon) \tag{13}$$

Υ being a dummy parameter and $\alpha_\Psi = k\alpha$ with $0 \leqslant k < 1$. The stress gradient of the plastic potential may be expressed as

$$\Psi_\sigma = \frac{3}{2}\frac{\mathbf{s}}{\bar{\sigma}} + \alpha_\Psi \mathbf{1} \tag{14}$$

and the flow rule

$$\mathbf{d}^p = \dot{\lambda}\left(\frac{3}{2}\frac{\mathbf{s}}{\bar{\sigma}} + \alpha_\Psi \mathbf{1}\right) \tag{15}$$

The solution of the above equations must be subjected to the Kuhn–Tucker complementary conditions

$$\dot{\lambda} \geqslant 0, \quad f \leqslant 0, \quad \dot{\lambda}f = 0 \tag{16}$$

and the consistency condition

$$\dot{\lambda}\dot{f} = 0 \tag{17}$$

2.1.4. Failure conditions

As proposed by Carney et al. (2006), there are two different pressure cut-off limits, the first one in tension P_T^{lim} and the other in compression P_C^{lim}. The ice is assumed to fail if

$$p < P_T^{lim} = -\frac{\sigma_T}{3} \tag{18}$$

or if

$$p > P_C^{lim} = \frac{\sigma_C}{3} \tag{19}$$

In both cases, the failure condition sets the deviatoric stress to zero and the pressure is allowed to be only greater or equal to zero; it is supposed that after failure the broken ice could only withstand hydrostatic compressive stresses. The distortion energy density U_{dist} stored in the ice at failure conditions $p = \sigma_C/3$, which is lost during the computation when the deviatoric stress is set to zero, can be easily calculated using the Eqs. (5) and (8)–(10). The ratio of this energy and the kinetic energy density $U_k = 1/2\rho v_0^2$ reveals that the loss is negligible in the range of strain rates developed during the impact ($U_{dist}/U_k \approx 10^{-3}$). In compression, pressure and volumetric strain are related by the bulk modulus K. The parameters for the ice appear in Table 1, which were taken from the available literature.

2.2. Integration algorithm

Within the finite element method, the integration process is local in space, it occurs at quadrature points of the finite elements. The incremental integration of the constitutive model is regarded as a strain-driven process, in which the total strain tensor increment at each quadrature point is given at a certain time and both the stress and the state variables should be updated. Within the frame of the corotational configuration, the return mapping algorithm is proposed to solve the above equations. A complete implicit formulation would lead to a substantial increase of the computational cost. Then a semi-implicit return mapping algorithm is

3

Table 1
Model parameters for ice.

Density	ρ	897.6 kg/m^3
Young's modulus	E	9.31 GPa
Poisson rate	v	0.33
Initial compressive strength	σ_{C0}	10.976 MPa
Compressive strain rate sensitivity	m	0.093783
Tensile strength	σ_{T0}	1.72 MPa
Internal friction factor	k	1.15

proposed to integrate the constitutive equations, in which the direction of inelastic flow is evaluated at time $n+1$, and the slope of both the yield function α and of the plastic potential α_{ψ} are evaluated at time n. Since the yield surface remains constant during the plastic return, the first iteration enables to determine the increment in the plastic multiplier and update the stress. Appendix A details the integration procedure proposed to implement the model in the finite element code LS Dyna.

3. Numerical solvers

Nowadays engineering applications need numerical tools to improve the design process reliability and decrease the design global cost. Commercial finite element codes offer different numerical solvers, to model continuum mechanics problems. Therefore, in this research three different integration methods, Lagrangian, arbitrary Lagrangian Eulerian (ALE) and smoothed particles hydrodynamic (SPH), have been evaluated in order to study its performance to simulate the behavior of the ice under high strain rates. These three solvers are usually applied to non linear problems, such as impact.

In order to validate the proposed numerical model, experimental test of ice under high strain rates are needed. For this purpose the experimental results obtained by Pereira et al. (2006) and presented by Carney et al. (2006) were chosen. In these tests, cylindrical ice projectiles were launched against a steel plate tied to a cell load, using a helium gas gun. The size of ice cylinders was 17.5 mm diameter and 42.2 mm in length; the circular steel plate used as target has 63.5 mm of diameter as is shown in Fig. 3. A test campaign was accomplished at different impact velocities; the main result of those tests was the load vs. time registered in the load cell, which is going to be used in the present work to validate the proposed model.

The Lagrangian finite element solver is one of the most commonly used in continuum mechanics. This method links the mesh and the material, which may cause excessive distortion and hence numerical instabilities in problems in which the material deforms considerably. The ALE approach combines the Lagrangian and Eulerian methods (in the latter the mesh is fixed in space and the material flows through it); it takes advantage of both integration methods, computational efficiency of the Lagrangian and the capability of allowing large deformation of the Eulerian. Finally the smoothed particles hydrodynamic is a meshless method, in which the material is represented as a discretized group of particles, which are linked by the material properties. These properties are weighted by a function of the distance between particles; the formulation of this method allows large deformations in the material. Fig. 4 shows examples of the three aforementioned meshes for an ice cylinder.

In this work, the numerical simulations are accomplished using the commercial finite element code LS Dyna v971 considering each of the parts that are involved in the test: steel plate, cell load and ice projectile. For the steel plate, due to the fact that no plastic deformation is observed during the test, elastic behavior and a Lagrangian mesh of 9000 hexahedrons is used. The behavior of the cell load is represented by a mass spring system, as proposed by Carney et al. (2006), to take into account the back panel and support stiffness; this system is composed by three spring elements and a concentrated mass (Fig. 5). The three aforementioned spatial discretization methods have been used to simulate the cylindrical ice projectile in order to compare the results. The Lagrangian mesh of the projectile uses 10000 hexahedron elements; the ALE mesh consists in 17680 hexahedron elements, part of them are void surrounding the ice projectile; finally the SPH model is composed by 57280 particles. In the three cases the mesh size was obtained after a mesh sensitivity process. In the Lagrangian mesh an erosion criteria based on a maximum value of 1.5 for the equivalent strain has been established to avoid numerical problems due to mesh distortion; the elements are removed when their velocity is close to zero, and hence the kinetic energy of the ice lost by this erosion is negligible. The ice material was modeled using the developed model, which was implemented in a user sub routine. The properties are presented in Table 1. Fig. 6 shows the impact sequence for the three integration methods. Regarding the SPH numerical solver, no tensile instability has been found. This kind of problem that affects this meshless method is easily detected because particles tend to group in clusters (Swegle and Jeff, 2000), which was not found in the simulations.

4. Numerical simulations and model validation

To evaluate the proposed material model for the ice, experimental and numerical results are compared in Figs. 7 and 8 which correspond to ice impacts at 152 m/s and 213 m/s respectively. These figures depict the time history of the force induced in the load cell for the three different integration methods analyzed. At
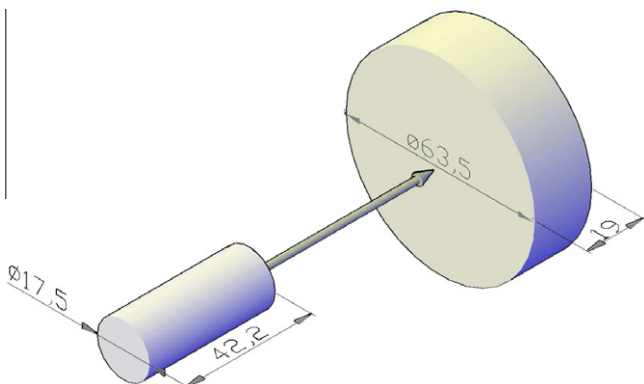

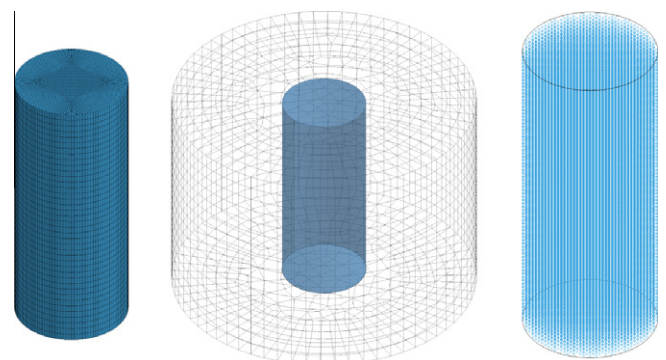**Fig. 3.** Sketch of the ice cylinder impactor and plate. Dimensions in mm.

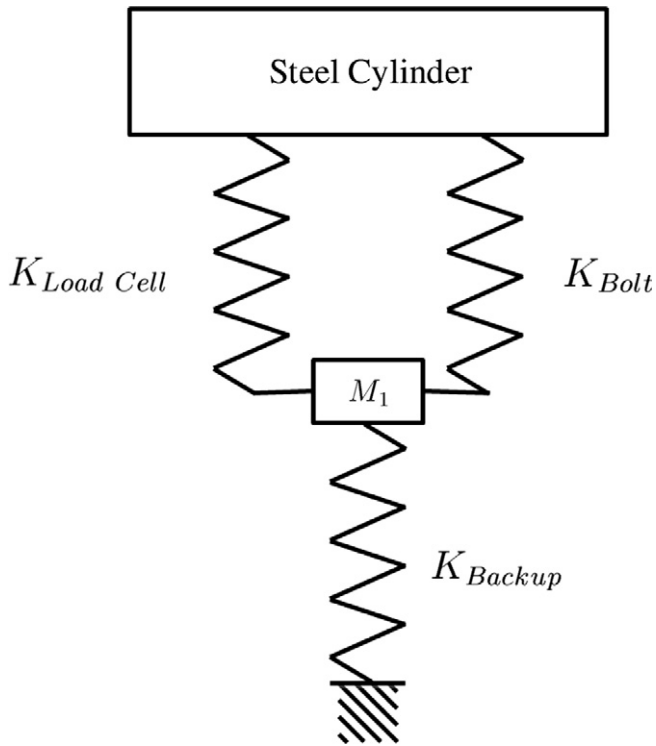**Fig. 4.** Numerical approaches: left Lagrangian, center ALE and right SPH.

4

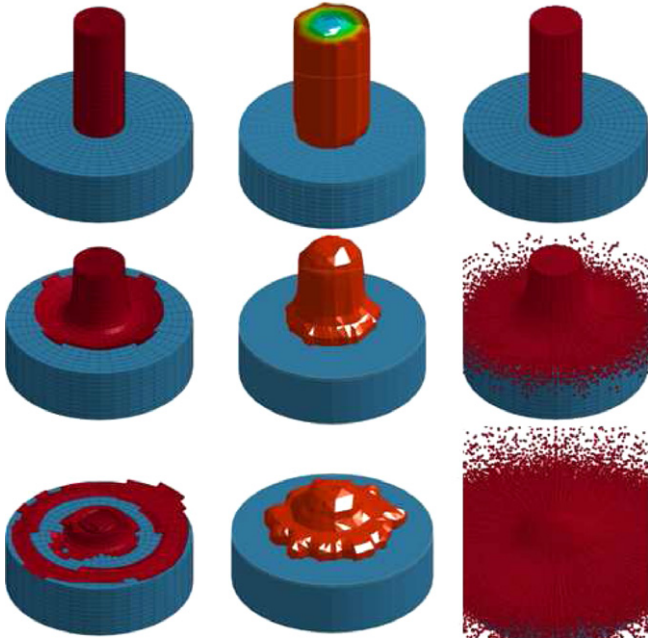**Fig. 5.** Masses and springs calculated to reproduce the experimental set-up (Carney et al., 2006).

Fig. 6. Impact sequence for the three integration procedures at $t = 0$ ms, $t = 0.087$ ms 0.176 ms. Left Lagrangian, center ALE and right SPH.
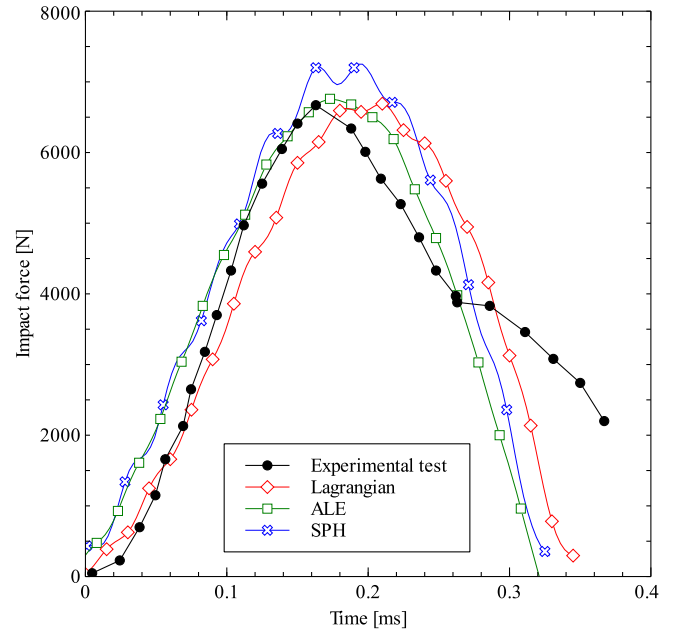

Fig. 7. Impact force vs. time curves; experimental and numerical results for the three numerical solvers. Impact velocity: 152 m/s.
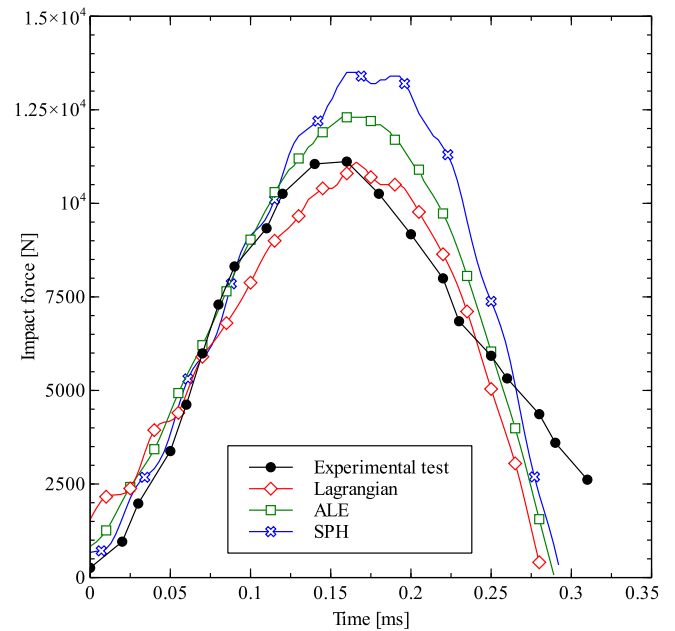

Fig. 8. Impact force vs. time curves; experimental and numerical results for the three numerical solvers. Impact velocity: 213 m/s.

152 m/s all integration methods show good results, giving an appropriate value for the maximum force and pulse extension; only the SPH integration method slightly overestimates this value respect to the experimental results. At higher velocity, 213 m/s, the Lagrangian integration method predicts faithfully the force in duced by the ice on the load cell, whereas the other two methods overestimate the maximum force, giving the ALE mesh a better

approach compared to the SPH. The lower values predicted by the Lagrangian method are possibly related with the erosion crite ria, which removes the element when a high level of strain is achieved (Heimbs, 2011). The three methods give appropriate re sults, being the Lagrangian the one that predicts the history of the force with more accuracy.

In order to analyze the differences between the three different integration methods, an analysis of the linear momentum transfer between the projectile and the plate is conducted. Fig. 9 shows the linear momentum for the ice and the target plate as function of time for an impact velocity of 152 m/s. Observing the Lagrangian case, is easy to note that the ice projectile is the one that less
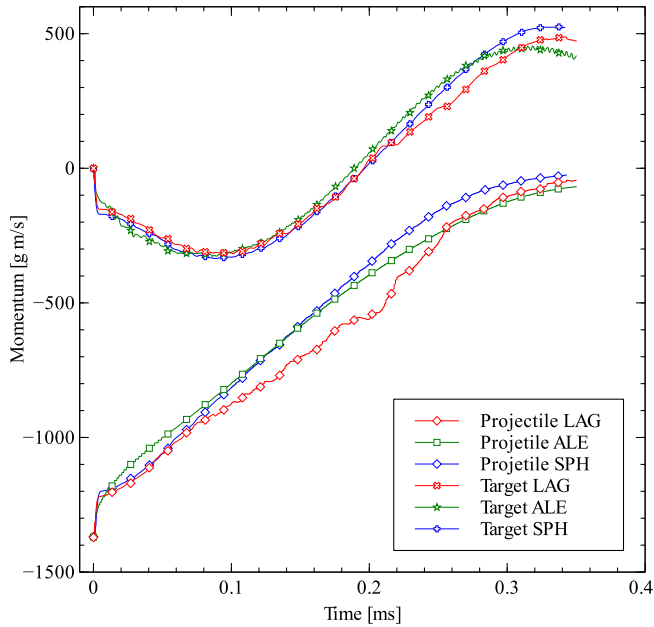
5

Fig. 9. Linear momentum in the impact direction vs. time curves for the ice projectile and the target plate for the three numerical solvers. Impact velocity: 152 m/s.

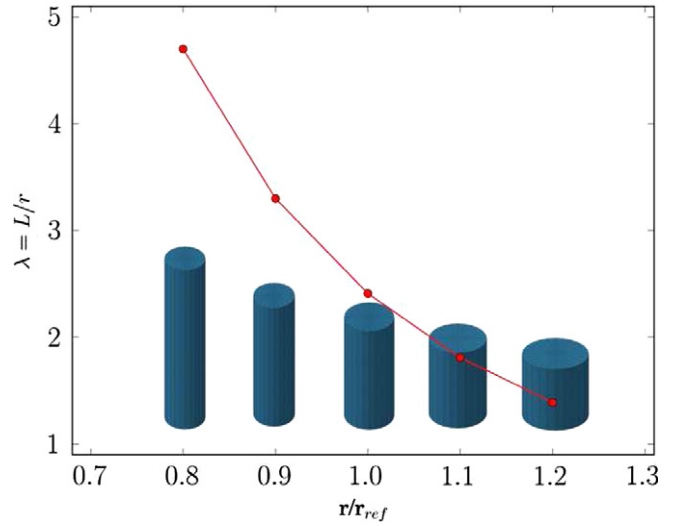**Fig. 10.** Slenderness comparison.

Fig. 11. Impact force vs. time for different slenderness values; impact velocity 213 m/s.

momentum loses, and correspondingly the target is the one to which less momentum is transferred (during the first 0.1 ms); this is in accordance with Fig. 7, in which the Lagrangian case exhibits the lowest impact force: less momentum transferred implies less force. In the SPH case, the momentum transferred to the target is the highest from $t = 0.08$ ms, which is in accordance to the maxi mum force found in the Fig. 7. Finally, the linear momentum trans ferred to the target in the ALE case, is the highest in the first instants, and the lowest onwards; this explains why the maximum of the impact force for this case occurs before the other two.

In order to obtain the optimal integration method in terms of computational cost and relative error, a comparison between the integration methods is shown in Table 2; in order to quantify the error, the maximum value of the force was used. The computa tional time is referred to the time of the fastest method, which is the Lagrangian for both studied impact velocities; this method is also the one that better approximates the experimental results, with errors below the 1%. The other two methods, ALE and SPH, re quire higher computational time (more that ten times) and have higher error predictions, being the SPH the worst one as aforementioned.

5. Analysis of the influence of the slenderness

Since the results of numerical simulations computed with Lagrangian method are the most accurate, this method is chosen to analyze the effect of the slenderness on the impact force, at

Table 2
Comparison of the three numerical solvers in terms of computational cost and error.

Method	Impact Vel. (m/s)	Relat. CPU time	Relat. error %
Lagrangian	152	t^{ref}_{152}	0.29
	213	t^{ref}_{213}	0.14
ALE	152	$10.97 \cdot t^{ref}_{152}$	1.34
	213	$10.25 \cdot t^{ref}_{213}$	10.65
SPH	152	$16.42 \cdot t^{ref}_{152}$	7.94
	213	$14.09 \cdot t^{ref}_{213}$	20.54
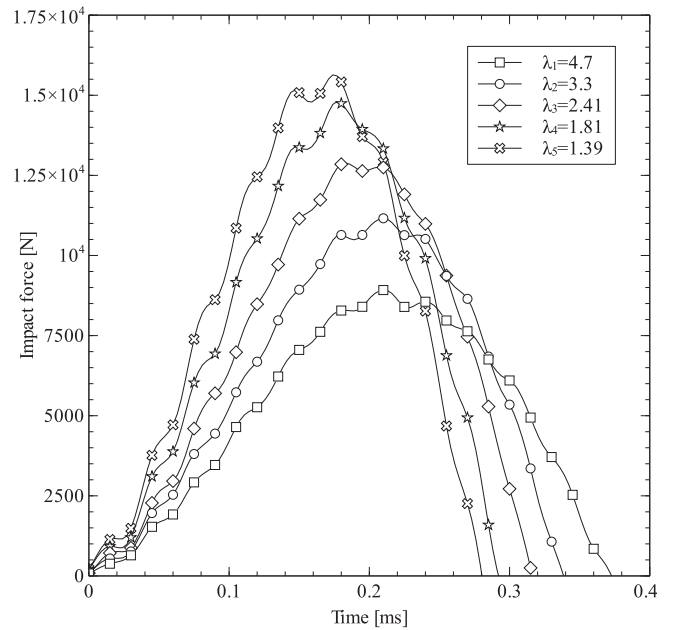
different velocities, keeping the total ice mass constant. Five differ ent slenderness (λ_V l/d, where l and d are the length and diame ter of the cylinder respectively) have been considered, being λ_V 2.41 the reference one, which has been previously validated with experimental tests. To complete the five cases to be analyzed, two different aspect ratios values below and above the reference value were chosen (Fig. 10). Those additional cases have not been compared with experimental results.

The impact force as a function of time for the different projec tiles is shown in Fig. 11 for impacts at 213 m/s. As the aspect ratio increases the maximum impact force diminishes and the instant in which the maximum impact force occurs is delayed. As it has been verified in the numerical simulations, the ice cylinder velocity does not change during the impact; hence the total time needed to completely splash against the load cell could be approximately
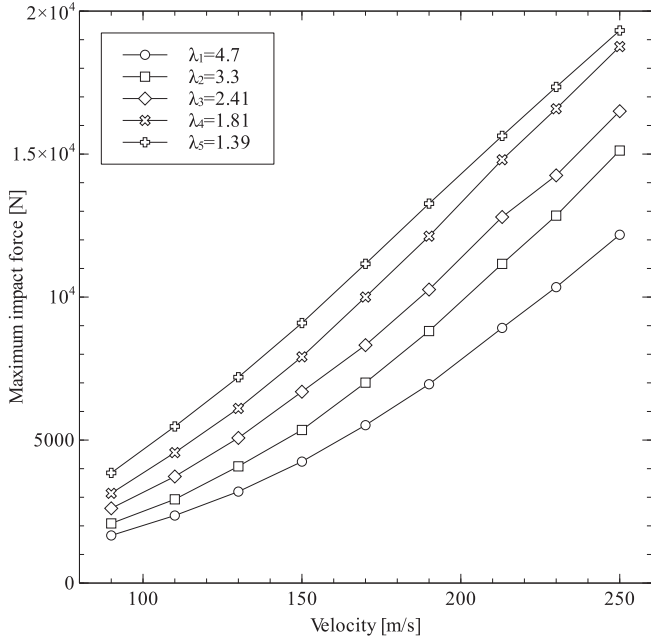
Fig. 12. Maximum impact force vs. impact velocity for different slenderness values.

estimated as $t_c \approx l/v$, being this time higher for the most slender cases; this fact explains the delay of the peak force as the slenderness increases. To explain the variation of the maximum force value with the aspect ratio, two effects must be considered; the first one is related to the area of the ice cylinder, as it increases (lower value of slenderness) the volume (and hence the mass) of ice impacted per unit of time increases, inducing in the plate a higher force value. In addition of this geometrical effect, there is another one related with the ice properties; as it has been stated before, the strength of the ice increases with the compression state, and due to the confinement effect, this compression is higher for the cases in which the aspect ratio is lower.

Fig. 11 shows results for a single impact velocity, at 213 m/s. In order to verify the dependence of the maximum impact force, for different impact velocities, Fig. 12 is plotted. In this graph it is possible to observe that the maximum impact force increases with impact velocity, and in addition for every impact velocity the most slender cylinders always gives lower values.

6. Conclusions

In this work a constitutive model to reproduce the behavior of the ice at high strain rates has been developed; the model is based on the Drucker–Prager yield criterion; the model has been implemented in a user subroutine to be use with the finite element code LS–DYNA. The model has been validated using experimental results obtained from the literature. Nevertheless it has to be noted that in order to asses a more strict validation of the constitutive model, additional experiments should be done because in this work it has been observed that the fracture energy is very small compared to the total kinetic energy. Three different integration methods have been studied to model the ice, Lagrangian, ALE and SPH; the developed model works properly with the three methods. All of them adequately reproduce the behavior of the ice in terms of the force induced during the impact, but the Lagrangian is the one that gives more accurate results with errors below 3%. Finally a parametric study has been performed, in order to study the influence of the slenderness of ice cylinders on the induced force during impact. It has been concluded that larger contact area end hence shorter cylinders promotes high impact loads.

Appendix A. Numerical integration of the constitutive model.

A.1. Constitutive model in a corotational frame

For the integration of the above set of nonlinear rate equations in a finite deformation frame, incremental objectivity is achieved by rewriting them in a corotational configuration (Simó and Hughes, 1998; Doghri, 2000a; Hagege, 2004). To formalize this approach, $\boldsymbol{\varpi}$ being a spatial skew symmetric tensor, a group of rotations $\Re$ can be generated so that

$$\dot{\Re} = \boldsymbol{\varpi}\Re, \quad \Re_{(t=0)} = \mathbf{1} \tag{A.1}$$

t being time, and with

$$\boldsymbol{\varpi} = -\boldsymbol{\varpi}^T \tag{A.2}$$

and

$$\Re^{-1} = \Re^T \tag{A.3}$$

Typical choices of $\boldsymbol{\varpi}$ include the spin tensor $\boldsymbol{w}$ and the tensor $\boldsymbol{\Omega}$ defined as

$$\boldsymbol{\Omega} = \dot{\boldsymbol{R}}\boldsymbol{R}^T \tag{A.4}$$

where $\boldsymbol{R}$ is the polar rotation tensor. The Cauchy stress tensor and the rate of deformation tensor are rotated as

$$\boldsymbol{\sigma}_\Re = \Re^T\boldsymbol{\sigma}\Re, \quad \mathbf{d}_\Re = \Re^T\mathbf{d}\Re \tag{A.5}$$

Time differentiation of the rotated Cauchy stress leads to

$$\dot{\sigma}_\Re = \Re^T(\dot{\boldsymbol{\sigma}} + \boldsymbol{\sigma}\boldsymbol{\varpi} - \boldsymbol{\varpi}\boldsymbol{\sigma})\Re = \Re^T\boldsymbol{\sigma}^\nabla\Re \tag{A.6}$$

Here, $\boldsymbol{\sigma}^\nabla$ coincides with the Jaumann stress rate if $\boldsymbol{\varpi} = \boldsymbol{w}$. The Hughes–Winget algorithm (1980) is used to compute $\Re$ in this case with an approximated formula valid for small increments. If $\boldsymbol{\varpi}$ is chosen to be equal to ω (and hence $\Re = \boldsymbol{R}$), $\boldsymbol{\sigma}^\nabla$ coincides with the Green–Naghdi–McInnis stress rate. Thus, a complicated objective stress rate can be computed as a simple time derivative. Taking advantage of the orthogonality of $\Re$, the symmetry of the Cauchy stress and rate of deformation tensors and the isotropy of the elastic tensor ($\mathbf{C}_\Re = \mathbf{C}$), the constitutive equations defined above, in which tensors are involved, are form identical in the corotational configuration but with spatial variables now replaced by rotated variables. Moreover, all the constitutive equations of the model involving only scalars remain unchanged.

The increment of total deformation in the corotational frame $\Delta\boldsymbol{\varepsilon}_\Re$, needed for the calculation of the trial stress (see Eq. (A.8) in following section) could be determined by an objective approximation of the rate of deformation tensor $\mathbf{d}_{n+1/2}$ calculated by the mid point rule (Simó and Hughes, 1998; Doghri, 2000a).

A.2. Discretization of the constitutive equations in the corotational frame

Within the finite element method, the integration process is local in space, it occurs at quadrature points of the finite elements. The incremental integration of the constitutive model is regarded as a strain driven process, in which the total strain tensor increment at each quadrature point is given at a certain time and both the stress and the state variables should be updated. Within the frame of the corotational configuration, the return mapping

7

algorithm is proposed to solve the above equations. If a Newton Raphson scheme is used to solve the set of non linear equations, a complete implicit formulation would lead to a substantial increase of the computational cost. Then a semi implicit return mapping algorithm is proposed to integrate the constitutive equations, in which the direction of inelastic flow is evaluated at time $n + 1$, and the slope of both the yield function α and of the plastic potential α_Ψ are evaluated at time n. The corresponding updated stress is then written as

$$\sigma_{n+1} = \sigma_{n+1}^{trial} + \Delta\sigma^{ret} \tag{A.7}$$

where trial stress is given by

$$\sigma_{n+1}^{trial} = \sigma_n + \mathbf{C} : \Delta\varepsilon \tag{A.8}$$

with σ_n being the stress at time n and $\Delta\varepsilon$ the increment of total deformation. The return stress $\Delta\sigma^{ret}$ is given by

$$\Delta\sigma^{ret} = \mathbf{C} : \Delta\varepsilon^p = \mathbf{C} : \Delta\lambda\left(\frac{3}{2}\frac{\mathbf{s}_{n+1}}{\sigma_{n+1}} + \alpha_\Psi\mathbf{1}\right)$$
$$= 3G\Delta\lambda\frac{\mathbf{s}_{n+1}}{\sigma_{n+1}} + 3K\alpha_\Psi\Delta\lambda\mathbf{1} \tag{A.9}$$

Then, the updated stress may be written as

$$\sigma_{n+1} = \sigma_{n+1}^{trial} - 3G\Delta\lambda\frac{\mathbf{s}_{n+1}}{\sigma_{n+1}} - 3K\alpha_\Psi\Delta\lambda\mathbf{1} \tag{A.10}$$

with $\Delta\lambda, \mathbf{s}_{n+1}$ and $\bar\sigma_{n+1}$ as unknowns. This last equation clearly shows the proportionality between $\mathbf{s}$ and $\mathbf{s}^{trial}$ (radial return), which could equally be stated as

$$\frac{\mathbf{s}_{n+1}}{\sigma_{n+1}} = \frac{\mathbf{s}_{n+1}^{trial}}{\sigma_{n+1}^{trial}} \tag{A.11}$$

Additional equations for the calculation of the unknowns are the yield condition $f = 0$ and the equation of the return stress (A.9); these last two equations must be solved simultaneously. Both equations are written in the form of residuals $\mathbf{R}_1$ and R_2 suitable for Newton Raphson iteration

$$\mathbf{R}_1 = \mathbf{C}^{-1} : \Delta\sigma^{ret} + \Delta\lambda\Psi_\sigma = 0 \tag{A.12}$$
$$R_2 = f(\sigma) = 0 \tag{A.13}$$

Linearization of these equations (considering that $\delta\sigma^{ret} = \delta\sigma$ if we begin the iteration from the trial state) gives

$$\mathbf{R}_1^{(i+1)} \approx \mathbf{R}_1^{(i)} + \mathbf{C}^{-1} : \delta\sigma^{(i)} + \Delta\lambda^{(i)}\left(\frac{\partial\Psi_\sigma}{\partial\sigma}\right)^{(i)} :$$
$$\delta\sigma^{(i)} + \delta\lambda^{(i)}\Psi_\sigma^{(i)} = 0 \tag{A.14}$$

$$R_2^{(i+1)} \approx R_2^{(i)} + \left(\frac{\partial f}{\partial\sigma}\right)^{(i)} : \delta\sigma^{(i)} = 0 \tag{A.15}$$

i being the subiteration index. These equations give $\delta\sigma^{(i)}$ and $\delta\lambda^{(i)}$. Solving for the plastic multiplier increment

$$\delta\lambda^{(i)} = \frac{R_2^{(i)} - \left(\frac{\partial f}{\partial\sigma}\right)^{(i)} : \mathbf{T}^{(i)} : \mathbf{R}_1^{(i)}}{\left(\frac{\partial f}{\partial\sigma}\right)^{(i)} : \mathbf{T}^{(i)} : \Psi_\sigma^{(i)}} \tag{A.16}$$

$\mathbf{T}^{-1}$ being the fourth order tensor

$$\mathbf{T}^{-1} = \mathbf{C}^{-1} + \Delta\lambda\frac{\partial\Psi_\sigma}{\partial\sigma} \tag{A.17}$$

From Eqs. (14) and (A.11) we see that the return direction remains constant during the iteration, so that Eq. (A.12) is lineal and $\mathbf{R}_1^{(i)} = 0$. Thus, expression (A.16) is written as

$$\delta\lambda^{(i)} = \frac{f_{n+1}^{(i)}}{\left(\frac{\partial f}{\partial\sigma}\right)^{(i)} : \mathbf{T}^{(i)} : \Psi_\sigma^{(i)}} \tag{A.18}$$

and $\delta\sigma^{(i)}$

$$\delta\sigma^{(i)} = -\delta\lambda^{(i)}\mathbf{T}^{(i)} : \Psi_\sigma^{(i)} \tag{A.19}$$

Tensor $\mathbf{T}$ can be easily computed considering that the Hessian of the plastic potential fits with the Hessian of the yield function in J_2 plasticity

$$\frac{\partial\Psi_\sigma}{\partial\sigma} = \frac{1}{\sigma}\left(\frac{3}{2}\mathbf{I}_{dev} - \mathbf{r}\otimes\mathbf{r}\right) \tag{A.20}$$

$\mathbf{I}_{dev}$ being the deviatoric projector

$$\mathbf{I}_{dev} = \mathbf{I} - \frac{1}{3}\mathbf{1}\otimes\mathbf{1} \tag{A.21}$$

with $\mathbf{I}$ the unit fourth order tensor

$$(\mathbf{I})_{ijkl} = \delta_{ik}\delta_{jl} \tag{A.22}$$

and $\mathbf{r}$ is the direction of the inelastic flow in J_2 plasticity given by the deviatoric tensor

$$\mathbf{r} = \frac{3}{2}\frac{\mathbf{s}}{\sigma} \tag{A.23}$$

Thus, applying the Sherman Morrison formula

$$\mathbf{T} = \mathbf{C} - \frac{6G^2\Delta\lambda}{3G\Delta\lambda + \sigma}\left(\mathbf{I}_{dev} - \frac{2}{3}\mathbf{r}\otimes\mathbf{r}\right) \tag{A.24}$$

Taking into account that the gradient of f is

$$\frac{\partial f}{\partial\sigma} = \frac{3}{2}\frac{\mathbf{s}}{\sigma} + \alpha\mathbf{1} \tag{A.25}$$

Eq. (A.18) is written as

$$\delta\lambda^{(i)} = \frac{f_{n+1}^{(i)}}{3G + 9K\alpha\cdot\alpha_\Psi} = \frac{f_{n+1}^{(i)}}{3G + 9K\alpha^2} \tag{A.26}$$

Since the yield surface remains constant during the return, the first subiteration enables us to determine $\Delta\lambda$ and the stress is updated by Eq. (A.10) considering the proportionality between $\mathbf{s}_{n+1}$ and $\mathbf{s}_{n+1}^{trial}$.

From the expression of the plastic return $\Delta\sigma^{ret}$ given by Eq. (A.9), we can easily determine its spherical and deviatoric components by projecting onto the axes $\{p, \bar\sigma\}$

$$\Delta p^{ret} = \frac{\Delta\sigma^{ret} : \mathbf{1}}{3} = 3K\Delta\lambda\alpha_\Psi \tag{A.27}$$

$$\Delta\sigma^{ret} = \left(\frac{3}{2}\frac{9G^2\Delta\lambda^2}{\left(\sigma_{n+1}^{trial}\right)^2}s_{n+1}^{trial} : s_{n+1}^{trial}\right)^{1/2} = 3G\Delta\lambda \tag{A.28}$$

and the slope of the return direction in the bidimensional space $\{p, \bar\sigma\}$ (Fig. 1) is given by

$$\kappa^{ret} = \frac{\Delta\sigma^{ret}}{\Delta p^{ret}} = \frac{G}{K\alpha_\Psi} \tag{A.29}$$

Finally, updated compressive stress (Eq. (10)) is then calculated with updated values of equivalent plastic strain rate

$$\dot\varepsilon_{n+1}^p = \sqrt{\frac{2}{3}\mathbf{d}_{n+1}^p : \mathbf{d}_{n+1}^p} = \dot\lambda_{n+1}\sqrt{1 + 2\alpha_\Psi^2} = \frac{\Delta\lambda}{\Delta t}\sqrt{1 + 2\alpha_\Psi^2} \tag{A.30}$$

References

Anghileri, Marco, Invernizzi, Fabio, Mascheroni, Marco, 2005. A survey of numerical models for hail impact analysis using explicit finite element codes. International Journal of Impact Engineering 31, 929–944.

Carney, K., Benson, D., Dubois, P., Lee, R., 2006. A phenomenological high strain rate model with failure for ice. International Journal of Solids and Structures 43 (25–26), 7820–7839, December.

Cole, D., 1988. Crack nucleation in polycrystalline ice. Cold Regions Science and Technology 15 (1), 79–87.

Combescure, A., Chuzel-Marmot, Y., Fabis, J., 2011. Experimental study of high-velocity impact and fracture of ice. International Journal of Solids and Structures 48 (20), 2779–2790.

Doghri, I., 2000a. Mechanics of Deformable Solids. Springer-Verlag, Berlin.

Drucker, Prager, 1952. Soil mechanics and plastic analysis or limit design. Quarterly Journal of Applied Mathematics X (2), 157–165.

Dutta, Piyush K. 1993. Compressive failure of polycrystalline ice under impact. In: International Offshore and Polar Engineering Conference.

Fasanella, Edwin L., Boitnott, Richard L. 2006, Technical Report, February, NASA.

Gold, Lorne W., 1988. On the elasticity of the ice plates. Canadian Journal of Civil Engineering (156), 1080–1084.

Hagege, B. 2004. Simulation du comportement mécanique des renforts fibreux en grandes transformations: application aux renforts tricotés. Ph.D. Thesis, ENSAM, Paris.

Haynes, F.D. 1978. Technical Report, July.

Heimbs, S., 2011. Computational methods for bird strike simulations: a review. Computers and Structures 89, 2093–2112.

Hughes, T., Winget, J., 1980. Finite rotation effects in numerical integration of rate constitutive equations arising in large-deformation analysis. International Journal of Numerical Methods in Engineering 15, 1862–1867.

Jirsek, M., Bazănt, Z.P., 2002. Inelastic Analysis of Structures. John Wiley & Sons, England.

Jones, Stephen J., 1982. The confined compressive strength of polycrystalline ice. Journal of Glaciology 28 (98), 171–177.

Jones, Stephen J., 1997. High strain-rate compression tests on ice. The Journal of Physical Chemistry B 101 (32), 6099–6101. August.

Khan, A.S., Huang, S., 1995. Continuum Theory of Plasticity. John Wiley & Sons, N.Y.

Kim, Hyonny, Keune, John N., 2000. Modeling hail ice impacts and predicting impact damage initiation in composite structures. AIAA Journal 38 (7), 1278–1288, July.

Kim, Hyonny, Keune, John N, 2007. Compressive strength of ice at impact strain rates. Journal of Materials Science, 2802–2806, full set September 2005.

Kim, Hyonny, Welch, Douglas A., Kedward, Keith T., 2003. Experimental investigation of high velocity ice impacts on woven carbon/epoxy composite panels. Composites Part A 34, 25–41.

Kröner, E., 1959. Allgemeine kontinuumstheorie der versetzungen und eigen-spannungen. Archive for Rational Mechanics and Analysis 4, 273–334.

Lee, E.H., 1969. Elastic-plastic deformation at finite strains. Journal of Applied Mechanics 36, 1–6.

LSTC, Ls-Dyna KEYWORD USER'S MANUAL, Rev. 5, Livermore Software Technology Corporation, 2010. vol. I. Livermore, California.

Nemat-Nasser, S., 1982. On finite deformation elastoplasticity. International Journal of Solids and Structures 18, 857–872.

Park, Hwun, Kim, Hyonny, 2010. Damage resistance of single lap adhesive composite joints by transverse ice impact. International Journal of Impact Engineering 37 (2), 177–184.

Pereira, J. Michael, Padula, Santo A., Revilock, Duane M., Melis, Matthew E. 2006, Technical Report, July.

Petrovic, J.J., 2003. Mechanical properties of ice and snow. Journal of Material Science 38, 1–6.

Schulson, E., 1990. The brittle compressive fracture of ice. Acta Metallurgica et Materialia 38 (10), 1963–1976.

Schulson, E., 2001. Brittle failure of ice. Engineering Fracture Mechanics 68 (17–18), 1839–1887, December.

Shazly, Mostafa, Prakash, Vikas, Lerch, Bradley A. 2006, Technical Report, January.

Shazly, Mostafa., Prakash, Vikas., Lerch, Bradley A., 2009. High strain-rate behavior of ice under uniaxial compression. International Journal of Solids and Structures 46 (6), 1499–1515.

Sherburn, Jesse A., Horstemeyer, Mark F., 2010. International Journal of Impact Engineering Hydrodynamic modeling of impact craters in ice. International Journal of Impact Engineering 37 (1), 27–36.

Simó, J.C., Hughes, T.J.R., 1998. Computational Inelasticity. Springer-Verlag, New York.

Swegle, Jeff. 2000. Technical Report May.